CrystEngComm

PAPER

View Article Online
View Journal | View Issue

Cite this: *CrystEngComm*, 2015, **17**, 1654

Rietveld refinement, cluster modelling, growth mechanism and photoluminescence properties of $CaWO_4:Eu^{3+}$ microcrystals†

R. F. Gonçalves,*[a] L. S. Cavalcante,[b] I. C. Nogueira,[c] E. Longo,[d] M. J. Godinho,[de] J. C. Sczancoski,[d] V. R. Mastelaro,[f] I. M. Pinatti,[g] I. L. V. Rosa[g] and A. P. A. Marques[a]

Received 16th November 2014,
Accepted 3rd January 2015

DOI: 10.1039/c4ce02279c

www.rsc.org/crystengcomm

$CaWO_4:Eu^{3+}$ microcrystals (with 0, 1, 2 and 4 mol% Eu^{3+}) were synthesized by a co-precipitation (CP) method and grown in a microwave-assisted hydrothermal (MAH) system at 130 °C for 30 min. X-ray diffraction (XRD), Rietveld refinement, X-ray absorption near edge spectroscopy (XANES), Fourier-transform Raman (FT-Raman) and Fourier-transform infrared (FT-IR) spectroscopy indicated that all of the microcrystals have a scheelite-type tetragonal structure without deleterious phases. Structural refinement data were employed to model the [CaO_8], [EuO_8] and [WO_4] clusters. XANES spectra confirmed that the presence of deltahedral [EuO_8] clusters promotes small distortions of neighbouring tetrahedral [WO_4] clusters in a global tetragonal lattice. Field emission scanning electron microcopy (FE-SEM) images revealed that the replacement of Ca^{2+} by Eu^{3+} ions changed the particles' shapes, resulting in the different morphologies of the microcrystals. UV-vis diffuse reflectance spectra indicated a reduction in the optical band gap with the replacement of Ca^{2+} by Eu^{3+} ions. The photoluminescence (PL) properties of the Eu^{3+} ions in $CaWO_4$ were studied as well as the chromaticity coordinates and lifetimes of these compounds.

1. Introduction

In recent years, the continuous development of electronics has caused the electro-optical industry to search for new semiconductors with intense and well-defined luminescence emission for applications in lasers, light-emitting diodes, lamps, phosphors and displays.[1–4] In principle, the alkaline-earth metal tungstates belonging to the scheelite family, mainly calcium tungstate ($CaWO_4$), are potential candidates for these technological proposals.[5–7]

The studies on this oxide have been mainly focused on its photoluminescence (PL) response at room temperature. Thus, several research groups have been able to control the particle sizes and shapes of $CaWO_4$ to improve the efficiency or change the spectral range of its PL emission, which is commonly observed in the violet, blue and green regions of the visible electromagnetic spectrum.[8–10] Besides the morphological aspects, the optical phenomena of any semiconductor can be modified by introducing impurities or dopants into its crystalline lattice.[11,12]

$CaWO_4$, in particular, is one of the most efficient host matrixes for different rare-earth elements including neodymium, samarium, europium (Eu^{3+}), terbium, dysprosium and ytterbium.[13–16] Among them, Eu^{3+} is commonly employed as a dopant because of its intense and narrow emission lines extending from red to near-infrared when excited by ultraviolet wavelengths.[17,18] Besides being important for improving phosphor-based devices, its luminescence spectrum is highly structure-dependent, hence Eu^{3+} ions are considered to be a perfect sample for investigating microstructural changes in the crystalline environment.[19,20] Zhang *et al.*[21] reported the influence of several Eu^{3+} ion concentrations on the $CaWO_4$ microspheres synthesized *via* a precipitation method.

According to the authors, a 25% Eu^{3+} ion concentration (in molarity) is the optimum doping value for obtaining the maximum PL intensity, especially for those associated with $^5D_0 \rightarrow {}^7F_2$ transitions. Using the ethylene glycol route,

[a] *UNIFESP (Universidade Federal de São Paulo), Rua Prof. Artur Riedel, 275, Diadema, SP, CEP 09972-270, Brazil. E-mail: rosanaf.gon@gmail.com*
[b] *Departamento de Química, UESPI, CCN, Rua João Cabral, P.O. Box 2231, 64002-150, Teresina-PI, Brazil*
[c] *IFMA (Instituto Federal de Educação), Ciência e Tecnologia do Maranhão, PPGEM, São Luís, MA, Brazil*
[d] *LIEC-IQ, Universidade Estadual Paulista, P.O. Box 355, 14801-907, Araraquara, SP, Brazil*
[e] *Departamento de Química, CAC/UFG (Universidade Federal de Goiás), 75.704-020, Catalão, GO, Brazil*
[f] *IFSC, Universidade de São Paulo, P.O. Box 369, 13560 970, São Carlos, SP, Brazil*
[g] *CDMF-DQ, Universidade Federal de São Carlos, P.O. Box 676, 13565-905 São Carlos, SP, Brazil*

† Electronic supplementary information (ESI) available. CCDC 1032997–1033000. For ESI and crystallographic data in CIF or other electronic format see DOI: 10.1039/c4ce02279c

Sharma *et al.*[18] analysed the effect of heat treatment temperature on Eu^{3+}-doped $CaWO_4$ nanopowders with different Eu^{3+} ion concentrations. Chen *et al.*[22] showed that the particle shapes of Eu^{3+}-doped $CaWO_4$ depend on the pH and reaction time in a hydrothermal environment.

Various synthetic approaches have been used to manipulate the sizes, shapes and dimensions of pure and doped $CaWO_4$ microcrystals and nanocrystals such as the polymeric precursor method,[23] sonochemical synthesis,[24] solid-state reaction,[25] sol–gel processes,[26] the citrate complex route,[27] solvothermal methods,[28] conventional hydrothermal treatment (CHT)[29] and microwave-assisted hydrothermal processes (MAH).[30] Among these methodologies, MAH is a promising route with simple instrumentation, with CHT offering easy manipulation; however, this method uses microwave energy as the heat source for the reaction medium.[31,32] This type of synthesis has the advantages of preparing crystalline micromaterials and nanomaterials with low reaction temperatures, short holding times, mild reaction conditions, size-selective growth and controllable morphology. Basically, the particle formation and growth events in a hydrothermal environment are dependent on the temperature, time, pH, mineralizers and surfactants.[33]

The correlations between the optical phenomena and morphology of rare-earth doped $CaWO_4$ are ambiguous, and hence, this research area is an open field of investigation in materials science. Therefore, in the present paper, we investigated the optical properties and morphological aspects of $CaWO_4$:Eu^{3+} microstructures (with 0, 1, 2 and 4 mol% Eu^{3+}), synthesized by a co-precipitation (CP) method and grown in a microwave-assisted hydrothermal (MAH) system at 130 °C for 30 min. Different particle shapes were identified with increasing Eu^{3+} concentration, and a crystal growth mechanism was proposed in order to explain this behaviour. The PL profiles of $CaWO_4$:Eu^{3+} were influenced by the incorporation of Eu^{3+} in the lattice.

2. Experimental details

2.1. Synthesis and MAH processing of $CaWO_4$:Eu^{3+} microcrystals

$CaWO_4$:Eu^{3+} microcrystals (with 0, 1, 2 and 4 mol% Eu^{3+}) were synthesized by a CP method at room temperature using sodium tungstate(VI) dihydrate [$Na_2WO_4{\cdot}2H_2O$] (99% purity, Sigma-Aldrich), calcium acetate monohydrate [$Ca(CH_3CO_2)_2{\cdot}H_2O$] (99.5% purity, Aldrich) and europium(III) oxide [Eu_2O_3] (99.999% purity, Aldrich). First, $Na_2WO_4{\cdot}2H_2O$ was dissolved in 50 mL of deionized water under constant stirring. Europium(III) nitrate hexahydrate [$Eu(NO_3)_3{\cdot}6H_2O$] was prepared by the dissolution of Eu_2O_3 with four drops of nitric acid (65% Suprapur®, Merck) in a 10 mL aqueous solution to give a clear $Eu(NO_3)_3{\cdot}6H_2O$ solution. $Ca(CH_3CO_2)_2{\cdot}H_2O$ was dissolved in 50 mL of deionized water under constant stirring. The three other systems used for the preparation of $CaWO_4$:Eu^{3+} microcrystals (with 1, 2 and 4 mol% Eu^{3+}) were stoichiometrically prepared using 10 mL of each solution containing Eu^{3+} ions mixed with 40 mL of aqueous solutions containing Ca^{2+} ions. These four (Eu^{3+}/Ca^{2+} ions) solutions were added to those containing WO_4^{2-} ions, which were then sealed in a Teflon autoclave. The reactions of the Eu^{3+}/Ca^{2+} and WO_4^{2-} ions resulted in the formation of crystalline $CaWO_4$:Eu^{3+} precipitates, as shown in eqn (1)–(5) below:

$$Na_2WO_4{\cdot}2H_2O_{(s)} \xrightarrow{H_2O} 2Na^{+}_{(aq)} + WO_{4(aq)}{}^{2-} + 2H_2O \quad (1)$$

$$Ca(CH_3COO)_2{\cdot}H_2O_{(s)} \xrightarrow{H_2O} Ca_{(aq)}{}^{2+} + 2CH_3CO_{2(aq)}{}^{-} + H_2O \quad (2)$$

$$Eu(NO_3)_3{\cdot}6H_2O_{(s)} \xrightarrow{H_2O} Eu_{(aq)}{}^{3+} + 3NO^{-}_{3(aq)} + 6H_2O \quad (3)$$

After CP at room temperature,

$$Ca_{(aq)}{}^{2+} + WO_{4(aq)}{}^{2-} \xrightarrow{25\ ^\circ C} CaWO_{4(s)} \quad (4)$$

$$Ca_{(aq)}{}^{2+} + Eu_{(aq)}{}^{3+} + WO_{4(aq)}{}^{2-} \xrightarrow{25\ ^\circ C} (Ca,Eu)WO_{4(s)} \quad (5)$$

Finally, the Teflon autoclave was placed inside a microwave system (2.45 GHz, maximum power of 800 W). All of these systems were processed at 130 °C for 30 min. The heating rate in this system was fixed at 25 °C min^{-1}, and the pressure inside the autoclave was stabilized at 245 kPa. After processing, the autoclave was allowed to cool naturally to room temperature. The resulting suspension was washed with deionized water several times to neutralise the solution (pH ≈ 7). Finally, the white precipitates were collected and dried in a conventional furnace at 60 °C for several hours.

2.2. Characterization of $CaWO_4$:Eu^{3+} microcrystals

The $CaWO_4$:Eu^{3+} microcrystals were structurally characterized by XRD using a D/Max-2500PC diffractometer (Rigaku, Japan) with Cu Kα radiation (λ = 1.5406 Å) in the 2θ range from 10° to 75° at a scanning rate of 2° min^{-1} (exposure time of 33 min). The Rietveld routines were performed in the 2θ range from 10° to 110° at a scanning rate of 1° min^{-1} (exposure time of 100 min). The electronic and local atomic structure around the W atoms was determined by using the X-ray absorption spectroscopy (XAS) technique. The tungsten L_3-edge X-ray absorption spectra of the microcrystals were collected at the LNLS (National Synchrotron Light Laboratory) facility using the D04BXAFS1 beam line. XANES data were collected at W-L_3 in transmission mode at room temperature using a Si(111) channel-cut monochromator. For XAS spectra measurements, the samples were deposited on polymeric membranes and data were collected with the sample placed at 90° with respect to the X-ray beam. A XANES spectrum was recorded for each sample

using energy steps of 1.0 eV before and after the edge with 0.9 eV near the edge region for the L_3 edge. The FT-Raman spectra were recorded using an RFS100 spectrophotometer (Bruker, Germany) equipped with a Nd:YAG laser (λ = 1064 nm). The laser power on the sample was fixed at 100 mW and 500 scans were accumulated. The FT-IR spectra were recorded in the range of 200 to 1000 cm^{-1} with an MB-102 spectrophotometer (Bomem-Michelson, Switzerland) in transmittance mode. The crystal shapes and sizes were observed by field emission scanning electron microscopy (FE-SEM) using a Supra 35-VP microscope (Carl Zeiss, Germany) operated at 10 kV. UV-vis spectra were measured using a Varian (model Cary 5G, USA) spectrophotometer in diffuse reflection mode. PL measurements were performed using a MonoSpec27 monochromator from Thermo Jarrel Ash (USA) coupled to an R446 photomultiplier from Hamamatsu Photonics (Japan). A Coherent Innova 90K (USA) (λ = 350 nm) krypton ion laser was used as an excitation source, keeping its maximum output power at 500 mW and the maximum power on the sample after passing through an optical chopper was 40 mW. An optical parametric oscillator was employed for lifetime measurements. PL measurements were performed at room temperature.

3. Results and discussion

3.1. XRD analyses

Fig. 1(a–d) illustrate the XRD patterns of the $CaWO_4$:Eu^{3+} microcrystals (with 0, 1, 2 and 4 mol% Eu^{3+}) synthesized by the CP method at room temperature and processed in the MAH system at 130 °C for 30 min.

XRD was employed to evaluate the structural order–disorder at long-range and the lattice periodicity.[34] Fig. 1(a–d) indicate that all of the diffraction peaks are perfectly indexed to the scheelite-type tetragonal structure with the space group $I4_1/a$ (Inorganic Crystal Structure Database (ICSD) no. 18135).[35] Deleterious phases were not observed in the diffractograms.

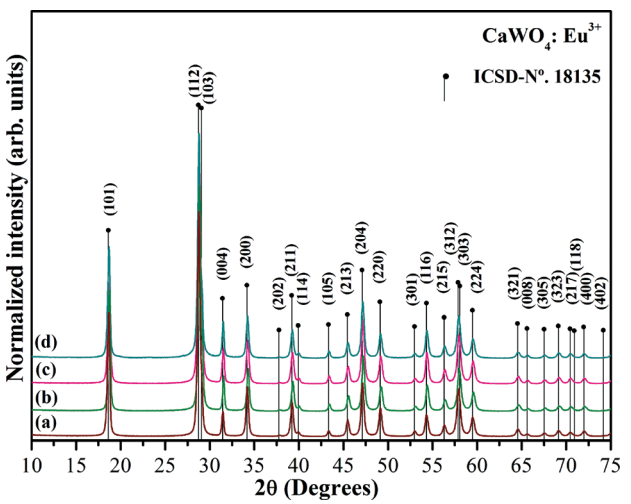

Fig. 1 XRD patterns of $CaWO_4$:Eu^{3+} microcrystals with various amounts of Eu^{3+}: (a) 0 mol%, (b) 1 mol%, (c) 2 mol% and (d) 4 mol%. The vertical lines indicate the relative positions of the diffraction peaks described in ICSD no. 18135.

As shown in Fig. 1(a–d), the presence of strong and sharp diffraction peaks is a typical characteristic of crystalline materials that are structurally ordered.[36]

3.2. Rietveld refinement analyses

The experimental lattice parameters, unit cell volumes, length of the links between (W–O)/(Ca–O)/(Eu–O) and the bond angles between (O–W–O)/(O–Ca–O)/(O–Eu–O) were obtained and calculated by the Rietveld refinement method[37] using the general structure analysis system (GSAS) program[38] with EXPGUI as the graphical interface.[39] The data obtained are shown in Tables S1, S2 and S3 in the ESI.†

Note that the values of the lattice parameters and unit cell volumes are very close to those published in the literature.[40–42] We have observed only small variations between these values, which can be related to the replacement of Ca^{2+} by Eu^{3+} ions, due to the difference in their electronic densities (Ca^{2+} ionic radius = 114 pm *vs.* Eu^{3+} ionic radius = 131 pm).[43] The peculiarity of each synthesis method, where the experimental variables (temperature, processing time, heating rate, solvents, *etc.*) influence the organization of [CaO_8], [EuO_8] and [WO_4] clusters within the scheelite structure, can cause the formation or reduction of structural defects (oxygen vacancies, distortion of the bonds, stresses and strains on the crystalline lattice) in the materials.[44] In previous work, we reported the presence of residual stresses and/or distortions in strontium and barium tungstates.[45,46]

The patterns calculated with some adjustments with respect to the observed pattern data provided the structural parameters of the material and the diffraction profile. In this work, the Rietveld method was applied to adjust cell and other parameters such as lattice parameters, atomic positions and occupancies.[47] In these analyses, the refined parameters were the scale factor, background, shift lattice constants, profile half-width parameters (u, v, w), isotropic displacement parameters, lattice parameters, strain anisotropy factors, preferred orientations, occupancies and atomic functional positions. The background was corrected using a Chebyshev polynomial of the first kind.[48] A peak profile function was modelled using a convolution of the Thompson–Cox–Hastings pseudo-Voigt (pV-TCH)[49] function with the asymmetry function described by Finger *et al.*,[50] which accounts for the asymmetry owing to axial divergence. To account for the anisotropy in the half-width of the reflections, the model by Stephens[51] was employed.

Fig. 2(a–d) illustrate the Rietveld refinement plots for the observed patterns *versus* the calculated patterns of the $CaWO_4$:Eu^{3+} microcrystals synthesized by the CP method at room temperature and processed in the MAH system at 130 °C for 30 min.

The results obtained by the Rietveld refinement method show good agreement between the observed XRD patterns and theoretical results (Fig. 2(a–d)). Moreover, the profiles of the XRD patterns experimentally observed and theoretically calculated display small differences between the observed y-scale values (Y_{obs}) and calculated y-values (Y_{calc}) on the

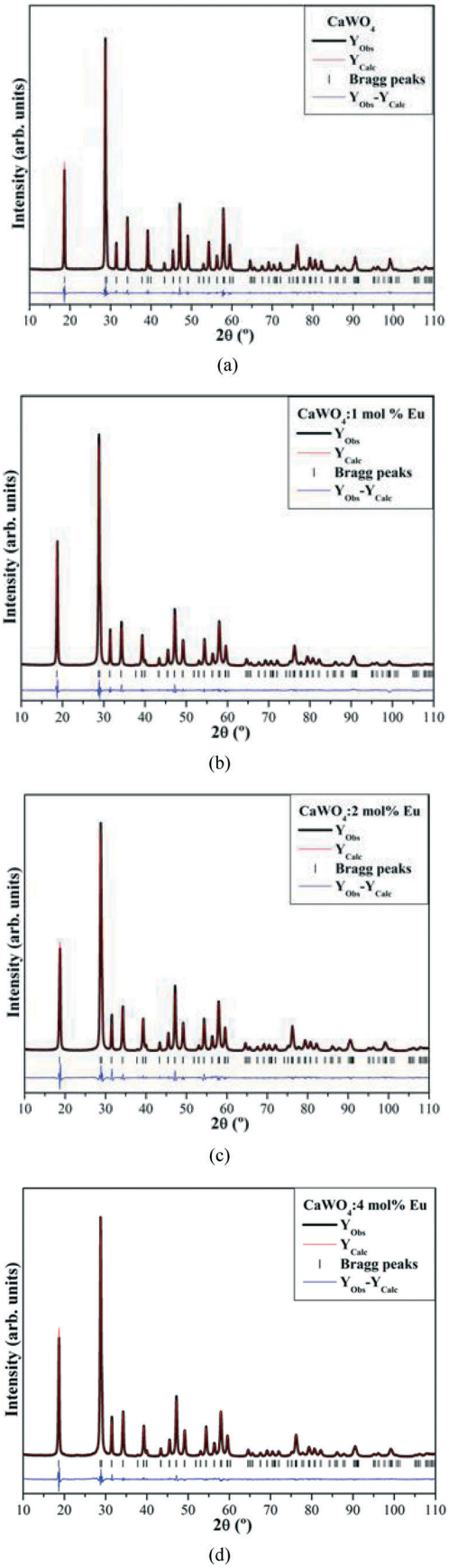

Fig. 2 Rietveld refinements of $CaWO_4:Eu^{3+}$ microcrystals with various amounts of Eu^{3+}: (a) 0 mol%, (b) 1 mol%, (c) 2 mol% and (d) 4 mol%.

intensity scale near zero, as illustrated by the (Y_{Obs} − Y_{Calc}) line. Shown in Table S1† are the fit parameters (R_{wp}, R_p, R_{Bragg} and χ^2) which suggest that the refinement results are very reliable (ESI,† Table S1). It is interesting to note that there are considerable variations in the atomic positions of the oxygen atoms, while the calcium and tungsten atoms kept their positions fixed within the structure. These results indicate the existence of structural distortions of the deltahedral [CaO_8]/[EuO_8] clusters and tetrahedral [WO_4] clusters in the $CaWO_4:Eu^{3+}$ microcrystals, which can be induced by the different levels of coupling between microwave radiation and the clusters.

3.3. Unit cell representations of $CaWO_4:Eu^{3+}$ microcrystals

The lattice parameters and atomic positions obtained by Rietveld refinement presented in Table S1 (ESI†) were used to model the pure tetragonal $CaWO_4$ structure (Fig. 3(a)) and the (Ca, Eu)WO_4 microcrystals (Fig. 3(b)).

These unit cells were modelled using the visualization for electronic and structural analysis (VESTA) program version 3.1.8 for Windows[52] using lattice parameters and atomic positions obtained from the Rietveld refinement data. $CaWO_4$ crystals are scheelite-type tetragonal structures with the space group $I4_1/a$, a point group symmetry of C_{4h}^6 and four asymmetric units per unit cell (Z = 4).[53] Fig. 3(a) illustrates that the bonds between O–W–O and O–Ca–O atoms are projected out of the structure. In these unit cells, tungsten (W) atoms are coordinated with four oxygen atoms to form tetrahedral [WO_4] clusters, with the symmetry group T_d.[54] These tetrahedral [WO_4] clusters are slightly distorted in the lattice and in each of the $CaWO_4:Eu^{3+}$ microcrystals. The differences in the O–W–O bond angles can lead to different levels of order–disorder and/or distortions in the $CaWO_4:Eu^{3+}$ crystal lattice (see Fig. 3(b)). We believe that this behaviour, shown by the Rietveld refinement data, could be due to the effect of partial replacement of Ca^{2+} by Eu^{3+} ions in the tetragonal $CaWO_4$ crystal lattice. In addition, in all unit cells, calcium (Ca) atoms are bonded to eight oxygen atoms, which results in the formation of [CaO_8] clusters with a deltahedral configuration, a D_{2d} symmetry group and a snub disphenoid polyhedral shape (8 vertices, 12 faces and 18 edges).[55] Thus, the [EuO_8] clusters have the same electronic coordination as the [CaO_8] clusters in the A-site. Moreover, we can verify possible distortions in the [CaO_8] clusters through the different bond angles between the O–Ca–O atoms, as presented in Table S3 (ESI†).

3.4. XANES spectra analyses

Fig. 4(a–e) illustrate the XANES spectra of the $CaWO_4:Eu^{3+}$ microcrystals synthesized by the CP method at room temperature and processed in the MAH system at 130 °C for 30 min.

The analyses performed on the XANES spectra can provide qualitative and/or semi-quantitative information on the chemical coordination (tetrahedral, square-based pyramidal, octahedral, *etc.*), the spatial arrangement of the atoms surrounding the absorber atom, the oxidation state and the density of

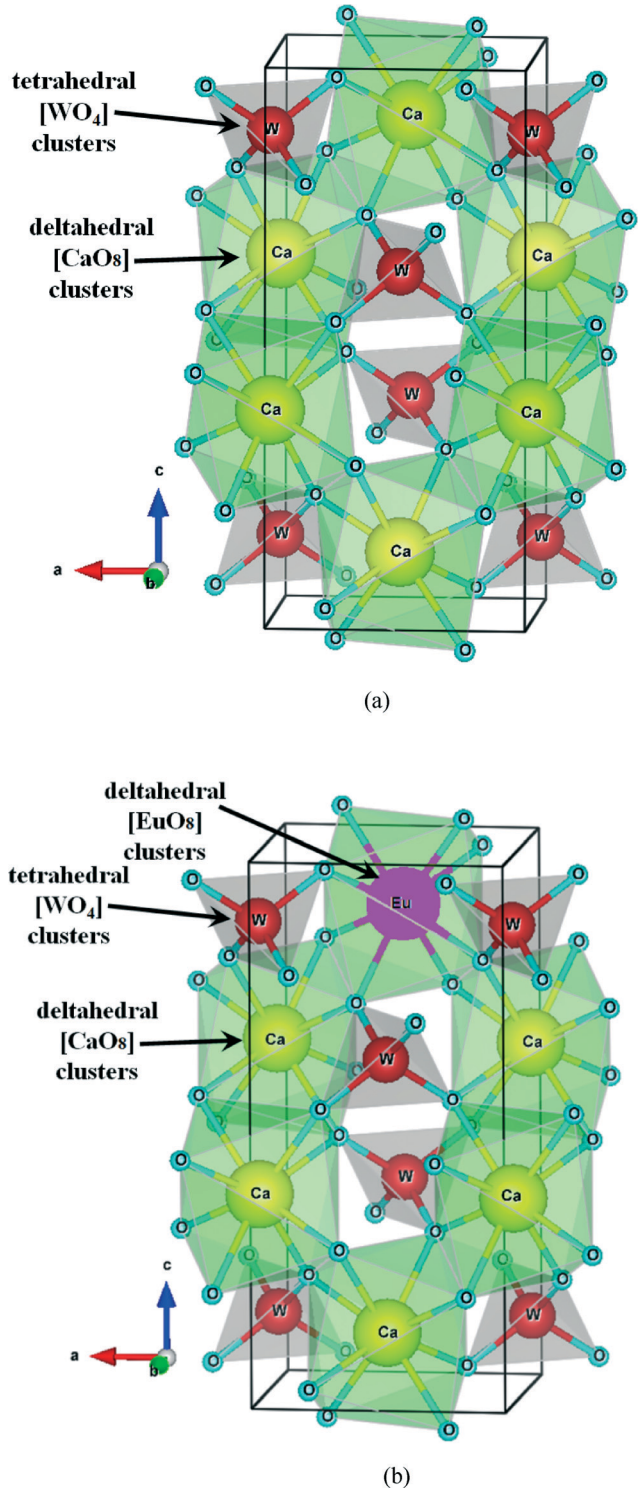

Fig. 3 Unit cell representations of (a) pure and (b) Eu-doped $CaWO_4$.

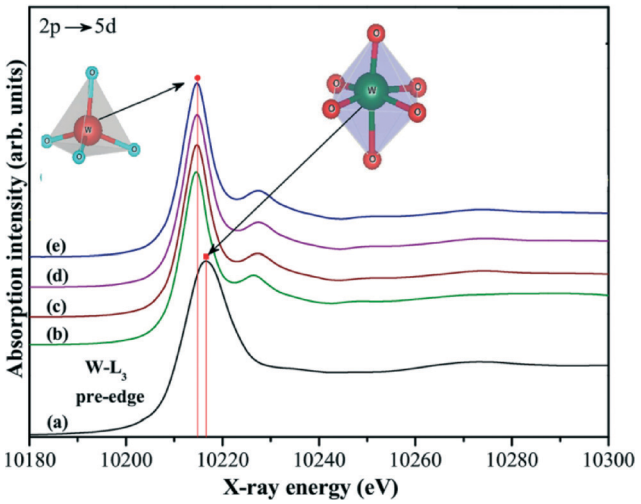

Fig. 4 XANES spectra of (a) WO_3 (standard sample) and $CaWO_4:Eu^{3+}$ microcrystals with various amounts of Eu^{3+}: (b) 0 mol%, (c) 1 mol%, (d) 2 mol% and (e) 4 mol%.

unoccupied states of the absorbing atom.[56] Moreover, we can use the XANES spectra to obtain information about the structural defects in oxides at short- and medium–range.[57]

As shown in Fig. 4(a), in the XANES spectrum at the W-L_3 edge for tungsten oxide (WO_3), which was used as a reference, there is a pre-edge peak (■) at approximately 10 216 eV. This position is different from those observed for the $CaWO_4:Eu^{3+}$ microcrystals (with 0, 1, 2 and 4 mol% Eu^{3+}) due to the W atoms coordinating with six oxygen atoms and displaying only distorted octahedral [WO_6] clusters with the symmetry group O_h. In Fig. 4(b–e), we can note a small shift of the pre-edge peak (●) for high values of X-ray energy, with the replacement of Ca^{2+} by Eu^{3+} ions, from 10 212 eV to 10 214 eV. It is reported in the literature[58] that the W-L_3 edge located at approximately 10 212 eV is ascribed to the permitted dipole transition from the $2p_{3/2}$(W) level to the quasi-bound mixed state 5d(W) + 2p(O), which is formed by the hybridisation of W 5d orbitals and O 2p orbitals. The presence of the pre-edge peak (●) in all $CaWO_4:Eu^{3+}$ samples is related to the distorted tetrahedral [WO_4] clusters (inset Fig. 4(b–e)) with the symmetry group T_d, which is characteristic of tungstates with a scheelite-type tetragonal structure.[59]

3.5. FT-Raman and FT-IR spectra analyses

Raman spectroscopy is considered to be a powerful tool for estimating the degree of structural order–disorder at short-range in oxide materials.[60] According to group theory calculations, tungstates with a scheelite-type tetragonal structure exhibit 26 different Raman and infrared vibrational modes, which are given in eqn (6):[61,62]

$$\Gamma_{(\text{Raman+infrared})} = 3A_g + 5A_u + 5B_g + 3B_u + 5E_g + 5E_u \quad (6)$$

where A_g, B_g, and E_g are Raman-active vibrational modes. The A and B modes are non-degenerate, while the E modes are doubly degenerate. The subscripts 'g' and 'u' indicate the pairs under inversion in centrosymmetric $CaWO_4:Eu^{3+}$ crystals. A_g, B_g, and E_g Raman modes are the result of the motion of the clusters in the crystal lattice. Therefore, 13 Raman-active vibrational modes of the $CaWO_4:Eu^{3+}$ crystals are anticipated, as indicated in eqn (7):[63,64]

$$\Gamma_{(\text{Raman})} = 3A_g + 5B_g + 5E_g \quad (7)$$

According to Basiev *et al.*,[65] the vibrational modes observed in the Raman spectra of the tungstates are classified into two modes, external and internal modes. External vibration modes are related to lattice phonons, which correspond to $[CaO_8]$ and $[EuO_8]$ cluster motions with the point symmetry D_{2d} in rigid cell units. Internal vibrational modes are related to $[WO_4]$ cluster vibrations in the lattice (assuming the centre of mass is in a stationary state). Isolated tetrahedral $[WO_4]$ clusters have the cubic point symmetry T_d,[66] and their vibrations comprise four internal modes $[\nu_1(A_1)$, $\nu_2(E_1)$, $\nu_3(F_2)$ and $\nu_4(F_2)]$, one free rotation mode $[\nu_{f.r.}(F_1)]$ and one translational mode $[(F_2)]$. On the other hand, when tetrahedral $[WO_4]$ clusters are located in the scheelite lattice, their point symmetry is reduced to S_4.[67]

As illustrated in eqn (6), after excluding 13 Raman vibrational modes, we have 13 infrared vibrational modes as demonstrated by eqn (8):[68]

$$\Gamma_{(\text{Infrared})} = 5A_u + 3B_u + 5E_u \quad (8)$$

However, among the 13 infrared vibrational modes, some cannot be observed, such as the $1A_u$ and $1E_u$ infrared modes that correspond to the zero wavenumber of acoustic modes at the centre of the Brillouin zone, the $3B_u$ infrared modes are forbidden, and the rest are optical modes.[69] Therefore, only eight IR-active vibrational modes remain, namely the $4A_u$ modes that are perpendicular to the *c*-axis and the $4E_u$ modes with the electric vector parallel to the *c*-axis, as indicated in eqn (9):[70]

$$\Gamma_{(\text{Infrared})} = 4A_u + 4E_u \quad (9)$$

Fig. 5(a–d) illustrate the FT-Raman spectra of the $CaWO_4$:Eu^{3+} microcrystals synthesized by the CP method at room temperature and processed in the MAH system at 130 °C for 30 min.

In Fig. 5(a–d), only 11 of the 13 Raman active modes can be detected; no $1A_g$ or $1E_g$ Raman vibrational modes are observed. We believe that this behaviour is due to the low intensity of the modes, although Fig. 5(a–e) show that all of the FT-Raman spectra are well defined and have sharp peaks characteristic of materials with structural order at short-range.[71] However, other factors may produce different levels of structural order–disorder in the tetragonal lattice such as the preparation method, low temperature of synthesis/processing, geometry and/or crystal size. In our FT-Raman spectra, some Raman modes have small shifts that can be caused by distortions in the (O–W–O)/(O–Ca–O) bonds, interaction forces between $[WO_4]$–$[CaO_8]$–$[WO_4]$ clusters and/or different degrees of structural order–disorder in the lattice at short-range, which may be due to the replacement of Ca^{2+} by Eu^{3+} ions. Moreover, we have observed a slight broadening of the Raman peaks, which can be related to the reduction in the average crystal size. The inset in Fig. 5(a–d) depicts tetrahedral

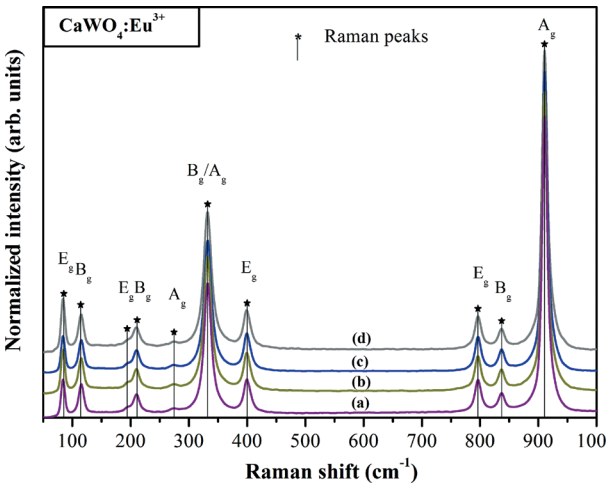

Fig. 5 Raman spectra of $CaWO_4$:Eu^{3+} microcrystals with various amounts of Eu^{3+}: (a) 0 mol%, (b) 1 mol%, (c) 2 mol% and (d) 4 mol%.

$[WO_4]$ clusters with symmetric stretching vibrations between O–W–O bonds. The relative positions of two of the Raman-active modes of the $CaWO_4$:Eu^{3+} crystals demonstrate a small shift in the free rotation $\nu_{f.r.}(F_1)$ Raman modes. These results can be linked to the effect of rare-earth ions which promotes different interactions between the $\cdots[WO_4]$–$[EuO_8]$–$[WO_4]\cdots$ clusters and/or $\cdots[WO_4]$–$[CaO_8]$–$[WO_4]\cdots$ clusters (see Fig. 3(a, b)), which is in good agreement with the literature.[72]

Fig. 6(a–d) illustrate the FT-IR spectra of the $CaWO_4$:Eu^{3+} microcrystals synthesized by the CP method at room temperature and processed in the MAH system at 130 °C for 30 min.

In our FT-IR spectra, only six of the eight IR active modes can be detected. The $1A_u$ and $1E_u$ IR modes could not be detected due to limitations of the FT-IR equipment. As discussed above, tungstates with a scheelite-type tetragonal structure show eight stretching and/or bending vibrational modes in their FT-IR spectra.[73,74] In our case, it was possible to identify no more than six modes $(2(A_u)$, $1(E_u)/1(A_u)$ and

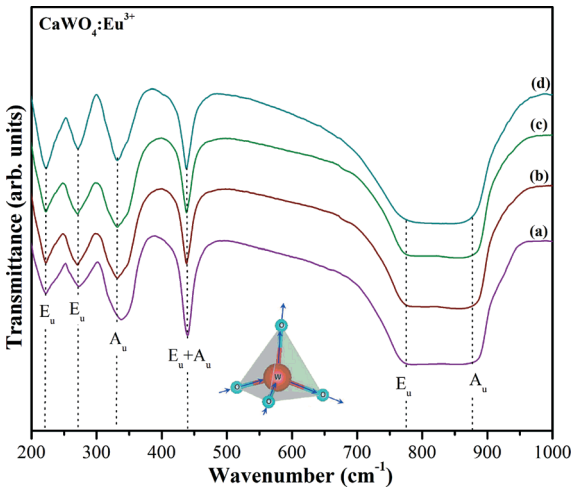

Fig. 6 FT-IR spectra of $CaWO_4$:Eu^{3+} microcrystals with various amounts of Eu^{3+}: (a) 0 mol%, (b) 1 mol%, (c) 2 mol% and (d) 4 mol%.

2(E_u)), which were identified at specific positions in the spectra (Fig. 6(a–e)). First, there are strong absorption bands with two modes located at 772/778 and 873/882 cm^{-1} for all $CaWO_4$:Eu^{3+} microcrystals. These two bands are related to the v_3(1E_u and 1A_u) internal modes originating from the anti-symmetric stretching vibrations in tetrahedral [WO_4] clusters.[75] Similarly, the other two v_4(1A_u and 1E_u) modes are assigned to the anti-symmetric bending of the bonds in [WO_4] clusters. These modes are located at approximately 438/440 cm^{-1} for the $CaWO_4$:Eu^{3+} microcrystals. Finally, the two other absorption bands located at 330/332 cm^{-1} and 268/270 cm^{-1} are ascribed to the v_2(1A_u mode) and the (1E_u mode). These modes refer to the symmetric bending of O–W–O bonds in tetrahedral [WO_4] clusters. In Fig. 6(a–f), the vertical lines are used as guides. Pure $CaWO_4$ microcrystals have infrared bands at slightly different positions with respect to the $CaWO_4$:Eu^{3+} microcrystals with 0, 1, 2 and 4 mol% Eu^{3+}. This behaviour can be related to the presence of crystals with very similar O–W–O bonds. Moreover, pure $CaWO_4$ microcrystals have similar energy coupling and bond strength of the ···O–W–O–Ca–O–W–O··· bonds in [WO_4]–[CaO_8]–[WO_4] clusters. However, the $CaWO_4$:Eu^{3+} microcrystals show the effect of environments linked to Eu^{3+} ions, promoting dispersion and bond strength variation between the ···O–W–O–Eu–O–W–O–Ca–O··· bonds in [WO_4]–[EuO_8]–[WO_4]–[CaO_8] clusters.

3.6. FE-SEM images analyses

Fig. 7(a–h) illustrate the FE-SEM images of the $CaWO_4$:Eu^{3+} microcrystals synthesized by the CP method at room temperature and grown in the MAH system at 130 °C for 30 min.

FE-SEM images were employed to monitor the shape evolution and growth process of the $CaWO_4$:Eu^{3+} microcrystals with partial replacement of Ca^{2+} by Eu^{3+} ions. Fig. 7(a) shows kibe-like $CaWO_4$ microcrystals for the pure system. These superstructures are composed of several aggregated nanocrystals, as noticed for an individual $CaWO_4$ microcrystal illustrated in Fig. 7(b). Moreover, we have obtained the values of average crystal size and lattice strain by Scherrer's equation using the full width at half maximum (FWHM) of the (101) peak from the XRD patterns (Fig. 1(a–d)) as shown in Table S4 in the ESI.† $CaWO_4$ microcrystals have an average size of approximately 2.4 μm. In Fig. 7(c–h), the effect of the replacement of Ca^{2+} with Eu^{3+} ions on the shape and size of the microcrystals can be noticed. The jackfruit-like $CaWO_4$:Eu^{3+} (1 mol%) microcrystals show a slight reduction in their average size to approximately 1.9 μm. The sample with 2 mol% Eu^{3+} shows drastic modification from a crystal shape to a dumbbell-like shape. In Fig. 7(g–h) a retraction process at the centres of the crystals can be observed, which is due the presence of Eu^{3+} ions in the $CaWO_4$ lattice. These microcrystals grow at their extremities and have an average size of approximately 1.7 μm. Finally, we can clearly observe the remarkable effects of Eu^{3+} ions on the growth process of the crystals, with the morphology close to twin lychee-like $CaWO_4$:Eu^{3+} microcrystals

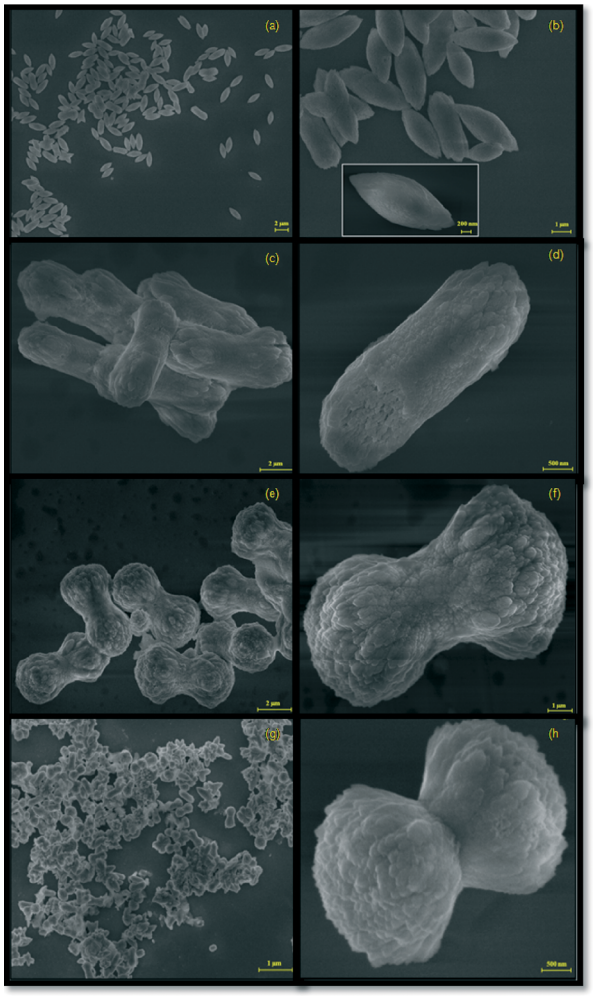

Fig. 7 FE-SEM micrographs of (a, b) kibe-, (c, d) jackfruit- (e, f) dumbbell- and (g, h) twin lychee-like $CaWO_4$:Eu^{3+} microcrystals.

(4 mol%) and an average size of approximately 1.5 μm. Generally, it is possible to deduce that the increase in Eu^{3+} ions in the compounds promotes a change in the growth process from anisotropic to isotropic, potentially reducing the size of the matrix crystals.

3.7. Growth mechanism of $CaWO_4$:Eu^{3+} microcrystals

Fig. 8(a–g) display a schematic representation of the main stages involved in the growth mechanism of the $CaWO_4$:Eu^{3+} microcrystals (with 0, 1, 2 and 4 mol% Eu^{3+}) obtained by the CP method at room temperature and processed at 130 °C for 30 min in the MAH system.

The initial process is the formation of small octahedron-like $CaWO_4$:Eu^{3+} crystals, which occurs with the addition of stoichiometric amounts of $Ca(CH_3CO_2)_2{\cdot}H_2O$, $Eu(NO_3)_3{\cdot}6H_2O$ and $Na_2WO_4{\cdot}2H_2O$ dissolved in deionized water (Fig. 8(a)). In this solution, the solvation energy of the H_2O molecules promotes rapid dissociation of the salts, where the Ca^{2+}, Eu^{3+} and WO_4^{2-} ions are rapidly solvated by surrounding H_2O molecules.[76,77] The partial negative charge on the H_2O

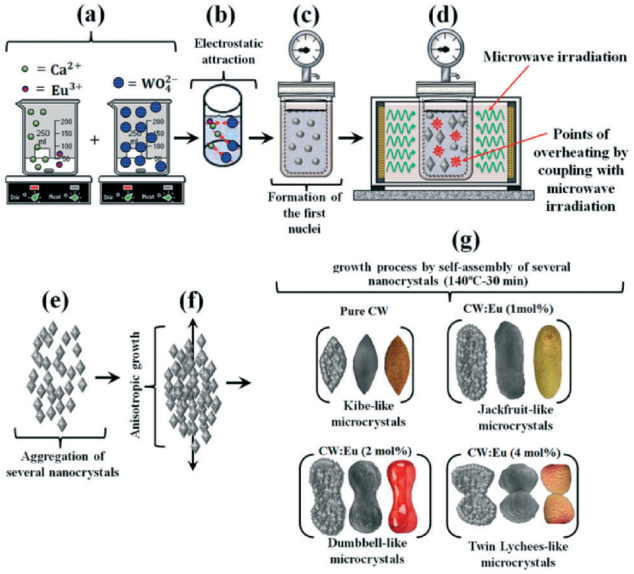

Fig. 8 Growth mechanisms of the $CaWO_4$:Eu^{3+} (CW:Eu) microcrystals.

molecules is electrostatically attracted to the Ca^{2+}/Eu^{3+} ions, while the partial positive charges on the H_2O molecules are electrostatically attracted to the WO_4^{2-} ions.[78] However, due to differences in the electronic density between Ca^{2+}/Eu^{3+} ions and WO_4^{2-} ions, a strong Coulombic electrostatic attraction occurs between them that results in the formation of the first $CaWO_4$:Eu^{3+} precipitates or nucleation seeds (Fig. 8(b)). Next, these suspensions were transferred to a Teflon autoclave (Fig. 8(c)), which was placed inside a domestic MAH system. This apparatus was developed by several modifications of a microwave oven (model NN-ST357WRPH Piccolo 22 L, Panasonic).[79,80] Inside this system, the high microwave frequency interacts with the permanent dipoles of the liquid phase (H_2O) initiating rapid heating *via* molecular rotation (Fig. 8(d)). Likewise, the permanent or induced dipoles in the dispersed phase promote rapid heating of the crystals.[81,82] The microwave radiation also promotes an increase in the effective collision rate between the particles in suspension, contributing to the crystal attachment and growth processes.[83] The adsorption of H_2O on the $CaWO_4$:Eu^{3+} crystal surfaces favours aggregation and diffusion of nanocrystals leading to fast growth of microcrystals, which are adhered by van der Waals forces.[84] Fig. 8(e, f) show the proposed growth mechanism responsible for the formation and growth of aggregated $CaWO_4$:Eu^{3+} crystals. Under MAH conditions, after formation of the first nuclei, self-organization and/or mutual aggregation occurs by uncountable collision events. The self-assembly mechanism and different charges between Eu^{3+} and Ca^{2+} ions in the crystal lattice are dominant in this case and lead to interactions between multiple octahedral nanocrystals to form crystals with different shapes (kibe-, jackfruit-, dumbbell- and twin lychee-like microcrystals), as shown in Fig. 8(g). Initially, the $CaWO_4$:Eu^{3+} crystals have a predominantly anisotropic growth, but with an increase in the amount of Eu^{3+} (2 and 4 mol%), there is a tendency for isotropic growth. This occurs due to unidirectional growth attributed to the different rates of interaction between the crystal surfaces, leading to a continuous growth mechanism on a specific surface.[85,86]

3.8. UV-vis diffuse reflectance spectroscopy analyses

The optical band gap energy (E_{gap}) values were calculated using the Kubelka–Munk equation,[87] which is based on the transformation of diffuse reflectance measurements, to estimate E_{gap} values with good accuracy.[88] Particularly, it is used in limited cases of infinitely thick samples. The Kubelka–Munk equation (eqn (10)) for any wavelength is described by:

$$\frac{K}{S} = \frac{(1-R_\infty)^2}{2R_\infty} \equiv F(R_\infty) \quad (10)$$

where $F(R_\infty)$ is the Kubelka–Munk function or the absolute reflectance of the sample. In our case, magnesium oxide (MgO) was adopted as the standard sample in the reflectance measurements, $R_\infty = R_{sample}/R_{MgO}$ (R_∞ is the reflectance), K is the molar absorption coefficient and S is the scattering coefficient. In a parabolic band structure, the optical band gap and the absorption coefficient of semiconductor oxides[89] can be calculated by eqn (11):

$$\alpha h\nu = C_1(h\nu - E_{gap})^n \quad (11)$$

where α is the linear absorption coefficient of the material, $h\nu$ is the photon energy, C_1 is a proportionality constant, E_{gap} is the optical band gap and n is a constant associated with different kinds of electronic transitions (n = 1/2 for a direct allowed transition, n = 2 for an indirect allowed transition, n = 1.5 for a direct forbidden transition and n = 3 for an indirect forbidden transition). According to the theoretical calculations reported in the literature,[90] $CaWO_4$ microcrystals exhibit an optical absorption spectrum governed by direct electronic transitions. In this phenomenon, after the electronic absorption process, electrons located in minimum energy states in the conduction band (CB) are able to return to maximum energy states of the valence band (VB), which are at the same points in the Brillouin zone.[90,91] Based on this information, the E_{gap} values of $CaWO_4$:Eu^{3+} microcrystals were calculated using n = 1/2 in eqn (11). Finally, using the diffuse reflectance function described in eqn (10) with $K = 2\alpha$, we obtained the modified Kubelka–Munk equation as indicated in eqn (12):

$$[F(R_\infty)h\nu]^2 = C_2(h\nu - E_{gap}) \quad (12)$$

Therefore, by finding the $F(R_\infty)$ value from eqn (10) and plotting a graph of $[F(R_\infty)h\nu]^2$ against $h\nu$, E_{gap} values were calculated for the $CaWO_4$:Eu^{3+} microcrystals by extrapolating the linear portion of the UV-vis curves.

Fig. 9(a–d) illustrate the UV-vis spectra of the $CaWO_4$:Eu^{3+} microcrystals (with 0, 1, 2 and 4 mol% Eu^{3+}) obtained by the

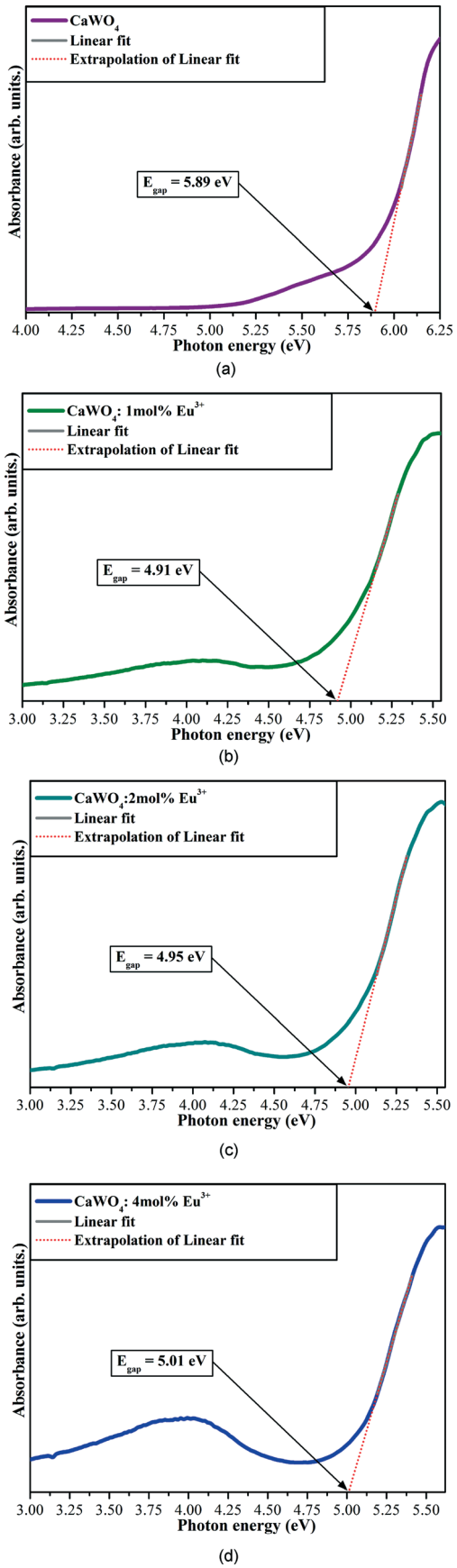

Fig. 9 UV-vis spectra of $CaWO_4$:Eu^{3+} microcrystals: (a) 0 mol%, (b) 1 mol%, (c) 2 mol% and (d) 4 mol%.

CP method at room temperature and processed at 130 °C for 30 min in the MAH system.

Fig. 9(a–d) indicate the tendency of the E_{gap} values to decrease with the replacement of Ca^{2+} by Eu^{3+} ions. This behaviour can be related to an increase in the intermediary energy levels between the VB and the CB. Moreover, the occurrence of this phenomenon can be explained to be due to the presence of new electronic levels related to the additional 4f orbitals of Eu^{3+} ions present in the microcrystal lattice. In addition, we believe that the E_{gap} values can also be related to factors such as morphology, particle shape and size as well as doping. In a recent study, Chen *et al.*[92] have successfully explained a correlation between the electronic structure and optical properties of Eu-doped ZnO crystals. Moreover, these authors have observed that the 4f orbitals are highly localized near the Fermi level of ZnO crystals. However, the existence of these electronic levels in our $CaWO_4$:Eu^{3+} microcrystals will be proven in a further paper by theoretical calculations.

3.9. PL emission, colorimetric data and lifetime analyses

Fig. 10(a, b) illustrate the PL emission spectra at room temperature (excited at 350.7 nm) and colorimetric data for $CaWO_4$:Eu^{3+} microcrystals (with 0, 1, 2 and 4 mol% Eu^{3+}) obtained by the CP method at room temperature and processed at 130 °C for 30 min in the MAH system. During the process of PL emission, we used a digital camera without flash (insets of Fig. 10(a)).

As observed in Fig. 10(a), the pure $CaWO_4$ microcrystals exhibit a broad PL emission band centred at around 525 nm in the blue-green region, which is assigned to the charge transfer transitions within the $[WO_6]$ octahedral groups in levels very close to the valence and conduction bands. This wide band shows the typical behaviour of multiphonon or multilevel processes, which involve the participation of numerous energy states within the band gap.[93]

However, with the partial replacement of Ca^{2+} by Eu^{3+} ions, a considerable decrease in this broad PL emission is observed (Fig. 10(a)). The blue-green emission is gradually quenched, and the narrow lines ascribed to Eu^{3+} emission are intensified. Probably, this behaviour is accompanied by an increase in the intermediary energy levels within the band gap, as indicated by the decrease in the band gap values, reported before in Fig. 9.

For the Eu^{3+}-doped $CaWO_4$ samples, the spectral profile observed is related to the dopant concentration in the matrix. The peaks are ascribed to the f–f transitions from the ground state to the excited states of Eu^{3+} ions. The emission spectrum of the Eu^{3+} ion shows the most intense emission lines corresponding to the $^5D_0 \rightarrow {}^7F_J$ (J = 0, 1, 2, 3, 4) transitions which occur in the range of 570–750 nm. The forbidden 'singlet–singlet' transition, $^5D_0 \rightarrow {}^7F_0$, is detectable and can be seen in the low wavelength region of the spectrum. The $^5D_0 \rightarrow {}^7F_1$ transition occurs by a forced magnetic dipole mechanism, and its intensity is not significantly altered by the perturbation of the crystalline field.[94,95]

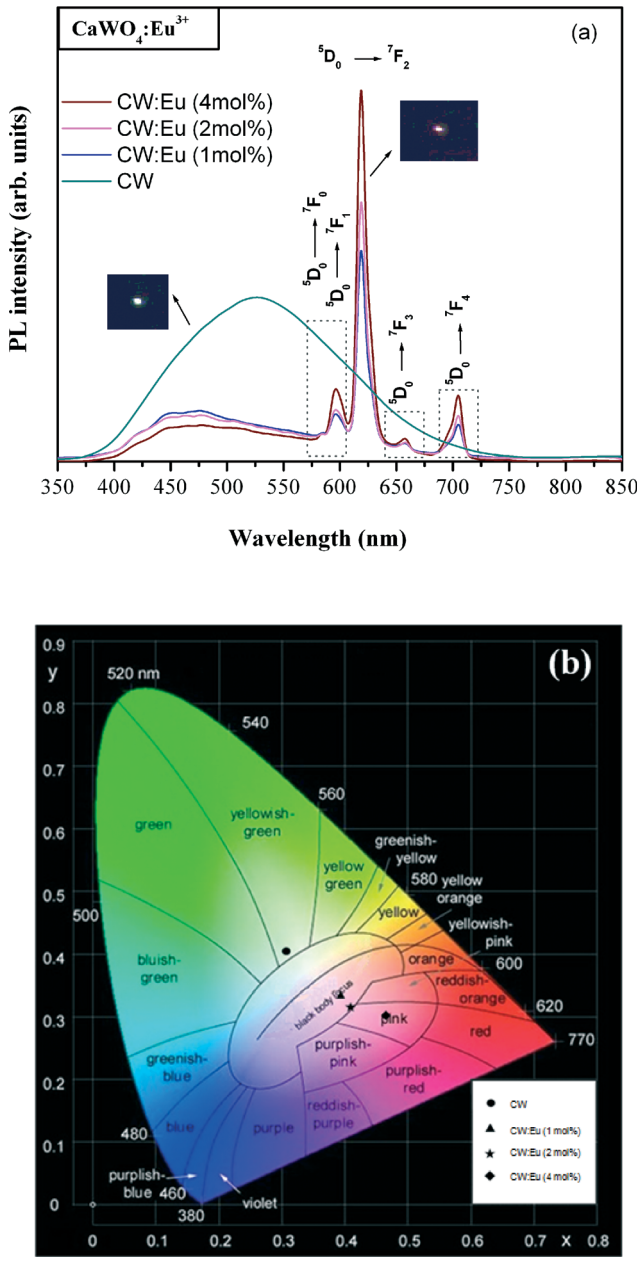

Fig. 10 (a) PL emission spectra at room temperature and (b) colorimetric data for $CaWO_4:Eu^{3+}$ (CW:Eu) microcrystals.

The $^5D_0 \rightarrow {}^7F_2$ transition at around 618 nm dominates the spectrum and is more intense than the other transitions. This is beneficial when phosphors with good colour purity are required. The intensity of the $^5D_0 \rightarrow {}^7F_2$ transition, which is known to be hypersensitive, is strongly dependent on the surrounding Eu^{3+} owing to its electric dipole characteristics. Here, the optimum europium concentration was found to be 4 mol% (Fig. 10(a)). We suggest that the relationship between the PL intensity and the amount of Eu^{3+} ions in the matrix is due to the coordination environment and/or changes in the shape and size of the crystals, since an increase of the Eu^{3+} concentration also leads to changes in the host morphology (Fig. 7). The literature has shown that the dipole–dipole interaction increases with an increase in the Eu^{3+} concentration, which consequently increases the cross-relaxation among Eu^{3+} ions when the mean distance between them is less than a critical value.[64] This critical value depends on the crystal structure of the host and the particle size.

Furthermore, defects in the crystal lattice play an important role in the determination of the luminescence properties of oxides. Therefore, the direct changing of the contents of some types of defects may cause variations in the concentrations of the corresponding luminescence centres.[96] In particular, the calcium and oxygen vacancies formed, which serve as electron- or hole-trapped centres, might act as sensitizers for the energy transfer from the host to the Eu^{3+} ions and enhance the luminescence intensity.

Fig. 10(b) shows the CIE (Commission Internationale de l'Eclairage) diagram for all of the $CaWO_4:Eu^{3+}$ microcrystals with various amounts of Eu^{3+} ((•) 0 mol%, (▲) 1 mol%, (★) 2 mol% and (♦) 4 mol%) with the respective assignment of their colours. The CIE chromaticity coordinates [x-axis, y-axis] for the $CaWO_4:Eu^{3+}$ microcrystals are [x = 0.3097, y = 0.4116], [x = 0.3934, y = 0.3400], [x = 0.4115, y = 0.3238] and [x = 0.4643, y = 0.3094], corresponding to Eu^{3+} concentrations of 0, 1, 2 and 4 mol%, respectively. Therefore, we can observe that the continuous replacement of Ca^{2+} by Eu^{3+} ions induces an increase in the maximum red PL emission, which has characteristic sharp lines due to 4f → 4f transitions in Eu^{3+} ions.[97,98]

The decay curves with their typical fitting were monitored for $CaWO_4:Eu^{3+}$ (with 1, 2 and 4 mol% Eu^{3+}). The respective lifetime (τ) values of the $^5D_0 \rightarrow {}^7F_2$ transitions were found to be τ = 0.43, 0.48 and 0.69 ms (ESI† Fig. S1(a–c)). The lifetime values increased with an increase in the Eu^{3+} concentration. These results are in good agreement with those obtained by other work reported in the literature, wherein preparations were carried out using a solid-state reaction method at 1100 °C for 6 h or a sol–gel method at 500 °C for 3 h.[99] However, we have obtained good results employing lower synthesis temperature.

4. Conclusions

In summary, we report the successful preparation of $CaWO_4:Eu^{3+}$ microcrystals using a facile microwave-hydrothermal method. XRD patterns, Rietveld refinement data, XANES and FT-Raman spectra indicate that all crystals have a scheelite-type tetragonal structure and are ordered at long- and short-range. The small difference in the ionic radii of Ca^{2+} and Eu^{3+} leads to substitution occurring in the A site occupied by calcium atoms.

The qualitative analyses of the XANES spectra of the crystals indicated that the coordination shell around the tungsten atoms is formed by four O atoms. FE-SEM images revealed that Eu^{3+} ions affect the shape and cause a reduction in the crystal size. The growth process proposed for these crystals indicates that growth occurs through the self-assembly of small nanocrystals, and further growth of intermediate superstructures and nanostructures leads to the

formation of kibe-, jackfruit-, dumbbell- and twin lychee-like crystals.

UV-vis diffuse reflectance spectra indicated that the replacement of Ca^{2+} by Eu^{3+} ions promotes a decrease in the optical band gap values due to the appearance of intermediary energy levels within the band gap. In principle, the $CaWO_4$ matrix exhibits broad PL emission in the blue-green region related to 2p–5d transitions, and after Eu^{3+} doping, $CaWO_4$ shows narrow PL emission in the red region ascribed to 4f–4f transitions (Eu^{3+} ions). Satisfactory lifetime values have been obtained for $CaWO_4$:Eu^{3+} microcrystals. The results suggest that our crystals have great potential for applications such as in phosphors, fluorescent lamps and display panels.

Acknowledgements

The authors acknowledge the financial support of the following Brazilian research funding institutions: the FAPESP (2013/07296-2), CNPq (304531/2013-8), National Laboratory of Synchrotron Light (D04B-XAFS1-11883) and CAPES.

Notes and references

1 Z. Ju, R. Wei, X. Gao, W. Liu and C. Pang, *Opt. Mater.*, 2011, **33**, 909–913.
2 R. Saraf, C. Shivakumara, N. Dhananjaya, S. Behera and H. Nagabhushana, *J. Mater. Sci.*, 2015, **50**, 287–298.
3 K. G. Sharma and N. R. Singh, *J. Lumin.*, 2013, **139**, 98–103.
4 A. J. Peter and I. B. Shameem Banu, *J. Mater. Sci.: Mater. Electron.*, 2014, **25**, 2771–2779.
5 J. Liu, Q. Wu and Y. Ding, *J. Cryst. Growth*, 2005, **279**, 410–414.
6 G. Andrzej, A. C. Wilson, H. Michael and S. Sander van, *J. Phys.: Condens. Matter*, 2003, **15**, 7261–7270.
7 M. A. M. A. Maurera, A. G. Souza, L. E. B. Soledade, F. M. Pontes, E. Longo, E. R. Leite and J. A. Varela, *Mater. Lett.*, 2004, **58**, 727.
8 L. Sun, M. Cao, Y. Wang, G. Sun and C. Hu, *J. Cryst. Growth*, 2006, **289**, 231–235.
9 Y. Wang, J. Ma, J. Tao, X. Zhu, J. Zhou, Z. Zhao, L. Xie and H. Tian, *Mater. Lett.*, 2006, **60**, 291–293.
10 Q. Zhang, W.-T. Yao, X. Chen, L. Zhu, Y. Fu, G. Zhang, L. Sheng and S. H. Yu, *Cryst. Growth Des.*, 2007, **7**, 1423–1431.
11 V. Lindroos, S. Franssila, M. Tilli, M. Paulasto-Krockel, A. Lehto, T. Motooka and V. M. Airaksinen, *Handbook of Silicon Based MEMS Materials and Technologies*, Elsevier Science, 2009.
12 W. Gao, Z. Li and N. M. Sammes, *An Introduction to Electronic Materials for Engineers*, World Scientific, 2011.
13 J. Sun, Y. Sun, C. Cao, Z. Xia and H. Du, *Appl. Phys. B: Lasers Opt.*, 2013, **111**, 367–371.
14 H. Y. He and Y. Wang, *J. Phys.: Condens. Matter*, 2013, **24**, 4847–4852.
15 C. Du, F. Lang, Y. Su and Z. Liu, *J. Colloid Interface Sci.*, 2013, **394**, 94–99.
16 Y.-L. Xu, Y.-L. Wang, L.-S. Shi and X. Tan, *Chin. Phys. Lett.*, 2013, **30**, 084207–084210.
17 F.-W. Kang, Y.-H. Hu, L. Chen, X.-J. Wang, H.-Y. Wu and Z.-F. Mu, *J. Lumin.*, 2013, **135**, 113–119.
18 K. G. Sharma, N. S. Singh, Y. R. Devi, N. R. Singh and S. D. Singh, *J. Alloys Compd.*, 2013, **556**, 94–101.
19 X. Cheng, C. Yuan, L. Su, Y. Wang and X. Zhu, *Opt. Mater.*, 2014, **37**, 214–217.
20 I. L. Rosa, A. P. Marques, M. T. Tanaka, D. M. Melo, E. R. Leite, E. Longo and J. A. Varela, *J. Fluoresc.*, 2008, **18**, 239–245.
21 Q. Zhang, Q. Meng and W. Sun, *Opt. Mater.*, 2013, **35**, 915–922.
22 Y. Chen, B. K. Moon, B. C. Choi, J. H. Jeong, H. K. Yang and P. Davies, *J. Am. Ceram. Soc.*, 2013, **96**, 3596–3602.
23 A. B. Campos, A. Z. Simões, E. Longo, J. A. Varela, V. M. Longo, A. T. de Figueiredo, F. S. De Vicente and A. C. Hernandes, *Appl. Phys. Lett.*, 2007, **91**, 051923–051925.
24 L. Yang, Y. Wang, Y. Wang, X. Wang and G. Han, *Adv. Powder Technol.*, 2013, **24**, 721–726.
25 F. Zhu, Z. Xiao, L. Yan, F. Zhang and A. Huang, *Appl. Phys. A: Mater. Sci. Process.*, 2010, **101**, 689–693.
26 L. Nadaraia, N. Jalabadze, R. Chedia, M. Antadze and L. Khundadze, *IEEE Trans. Nucl. Sci.*, 2010, **57**, 1370–1376.
27 H. Cho, S. M. Hwang, J. B. Lee, D. H. Ka, T. W. Kim, B. S. Lee, J. Y. Lee, J.-I. Lee and J. H. Ryu, *Trans. Nonferrous Met. Soc. China*, 2014, **24**, s134–s140.
28 T. J. Boyle, P. Yang, K. Hattar, B. A. Hernandez-Sanchez, M. L. Neville and S. Hoppe, *Chem. Mater.*, 2014, **26**, 965–975.
29 M. Wang, Y. Shi, Y. Tang and G. Jiang, *Mater. Lett.*, 2013, **109**, 12–15.
30 V. M. Longo, L. Gracia, D. G. Stroppa, L. S. Cavalcante, M. Orlandi, A. J. Ramirez, E. R. Leite, J. Andrés, A. Beltrán, J. A. Varela and E. Longo, *J. Phys. Chem. C*, 2011, **115**, 20113–20119.
31 J. C. Sczancoski, L. S. Cavalcante, M. R. Joya, J. A. Varela, P. S. Pizani and E. Longo, *Chem. Eng. J.*, 2008, **140**, 632–637.
32 D. P. Volanti, D. Keyson, L. S. Cavalcante, A. Z. Simoes, M. R. Joya, E. Longo, J. A. Varela, P. S. Pizani and A. G. Souza, *J. Alloys Compd.*, 2008, **459**, 537–542.
33 X.-Z. Wang, *J. Mater. Sci.: Mater. Electron.*, 2014, **25**, 3271–3275.
34 L. S. Cavalcante, J. C. Sczancoski, R. L. Tranquilin, M. R. Joya, P. S. Pizani, J. A. Varela and E. Longo, *J. Phys. Chem. Solids*, 2008, **69**, 2674.
35 R. D. Burbank, *Acta Crystallogr.*, 1965, **18**, 88–97.
36 S. M. M. Zawawi, R. Yahya, A. Hassan, H. N. M. E. Mahmud and M. N. Daud, *Chem. Cent. J.*, 2013, **7**, 80–89.
37 H. M. Rietveld, *J. Appl. Crystallogr.*, 1969, **2**, 65–71.
38 A. C. Larson and R. B. Von Dreele, *General Structure Analysis System (GSAS)*, Los Alamos National Laboratory, New Mexico, USA, Report LAUR, 2004, pp. 86–748.
39 B. H. Toby, *J. Appl. Crystallogr.*, 2011, **34**, 210–213.
40 A. Taoufyq, F. Guinneton, J.-C. Valmalette, M. Arab, A. Benlhachemi, B. Bakiz, S. Villain, A. Lyoussi, G. Nolibe and J.-R. Gavarri, *J. Solid State Chem.*, 2014, **219**, 127–137.

41 W. Hu, W. Tong, L. Li, J. Zheng and G. Li, *Phys. Chem. Chem. Phys.*, 2011, **13**, 11634–11643.
42 K. G. Sharma and N. R. Singh, *New J. Chem.*, 2013, **37**, 2784.
43 A. A. Reddy, S. Das, A. Goel, R. Sen, R. Siegel, L. Mafra, G. V. Prakash and J. M. F. Ferreira, *AIP Adv.*, 2013, **3**, 022126–022140.
44 L. S. Cavalcante, V. M. Longo, J. C. Sczancoski, M. A. P. Almeida, A. A. Batista, J. A. Varela, M. O. Orlandi, E. Longo and M. Siu Li, *CrystEngComm*, 2012, **14**, 853–868.
45 L. S. Cavalcante, J. C. Sczancoski, N. C. Batista, E. Longo, J. A. Varela and M. O. Orlandi, *Adv. Powder Technol.*, 2013, **24**, 344–353.
46 L. S. Cavalcante, J. C. Sczancoski, L. F. Lima Jr., J. W. M. Espinosa, P. S. Pizani, J. A. Varela and E. Longo, *Cryst. Growth Des.*, 2009, **9**, 1002–1012.
47 I. C. Nogueira, L. S. Cavalcante, P. F. S. Pereira, M. M. de Jesus, J. M. Rivas Mercury, N. C. Batista, M. S. Li and E. Longo, *J. Appl. Crystallogr.*, 2013, **46**, 1434–1446.
48 T. J. Rivlin, *The Chebyshev polynomials. Pure and Applied Mathematics*, New York-London-Sydney, 1974, ch. 2, pp. 56–123.
49 P. Thompson, D. E. Cox and J. B. Hastings, *J. Appl. Crystallogr.*, 1987, **20**, 79–83.
50 L. W. Finger, D. E. Cox and A. P. Jephcoat, *J. Appl. Crystallogr.*, 1994, **27**, 892–900.
51 P. W. Stephens, *J. Appl. Crystallogr.*, 1999, **32**, 281–289.
52 K. Momma and F. Izumi, *J. Appl. Crystallogr.*, 2011, **44**, 1272–1276.
53 A. Golubovic, R. Gajic, Z. Dohcevic-Mitrovic and S. Nikolic, *Sci. Sintering*, 2006, **38**, 265–272.
54 M. R. D. Bomio, L. S. Cavalcante, M. A. P. Almeida, R. L. Tranquilin, N. C. Batista, P. S. Pizani, M. Siu Li, J. Andres and E. Longo, *Polyhedron*, 2013, **50**, 532–545.
55 L. S. Cavalcante, F. M. C. Batista, M. A. P. Almeida, A. C. Rabelo, I. C. Nogueira, N. C. Batista, J. A. Varela, M. R. M. C. Santos, E. Longo and M. Siu Li, *RSC Adv.*, 2012, **2**, 6438–6454.
56 V. Krayzman, I. Levin, J. C. Woicik, D. Yoder and D. A. Fischer, *Phys. Rev. B: Condens. Matter Mater. Phys.*, 2006, **74**, 224104–224110.
57 M. Landmann, T. Kohler, E. Rauls, T. Frauenheim and W. G. Schmidt, *J. Phys.: Condens. Matter*, 2014, **26**, 253201–253245.
58 V. L. Aksenov, M. V. Kovalchuk, A. Y. Kuzmin, Y. Purans and S. I. Tyutyunnikov, *Crystallogr. Rep.*, 2006, **21**, 908–935.
59 S. Basu, B. S. Naidu, B. Viswanadh, V. Sudarsan, S. N. Jha, D. Bhattacharyya and R. K. Vatsa, *RSC Adv.*, 2014, **4**, 15606–15612.
60 V. S. Marques, L. S. Cavalcante, J. C. Sczancoski, E. C. Paris, J. M. C. Teixeira, J. A. Varela, F. S. De Vicente, M. R. Joya, P. S. Pizani, M. Siu Li, M. R. M. C. Santos and E. Longo, *Spectrochim. Acta, Part A*, 2009, **74**, 1050–1059.
61 T. T. Basiev, A. A. Sobol, Y. K. Voronko and P. G. Zverev, *Opt. Mater.*, 2000, **15**, 205–216.
62 Z. C. Ling, H. R. Xia, D. G. Ran, F. Q. Liu, S. Q. Sun, J. D. Fan, H. J. Zhang, J. Y. Wang and L. L. Yu, *Chem. Phys. Lett.*, 2006, **426**, 85–90.
63 Y. Chen, S. W. Park, B. K. Moon, B. C. Choi, J. H. Jeong and C. Guo, *CrystEngComm*, 2013, **15**, 8255–8261.
64 K. G. Sharma and N. R. Singh, *J. Rare Earths*, 2012, **30**, 310–314.
65 T. T. Basiev, A. A. Sobol, P. G. Zverev, L. I. Ivleva, V. V. Osiko and R. C. Powell, *Opt. Mater.*, 1999, **11**, 307–314.
66 Y. K. Voronko and A. A. Sobol, *Inorg. Mater.*, 2005, **41**, 420–428.
67 P. F. S. Pereira, A. P. de Moura, I. C. Nogueira, M. V. S. Lima, E. Longo, P. C. de Sousa Filho, O. A. Serra, E. J. Nassar and I. L. V. Rosa, *J. Alloys Compd.*, 2012, **526**, 11–21.
68 A. Golubovic, R. Gajic, Z. Dohcevic-Mitrovic and S. Nikolic, *J. Alloys Compd.*, 2006, **415**, 16–22.
69 R. Vali, *Comput. Mater. Sci.*, 2011, **50**, 2683–2687.
70 J. Guo, D. Zhou, Y. Li, T. Shao, Z.-M. Qi, B.-B. Jinc and H. Wang, *Dalton Trans.*, 2014, **43**, 11888–11896.
71 J. C. Sczancoski, L. S. Cavalcante, M. R. Joya, J. W. M. Espinosa, P. S. Pizani, J. A. Varela and E. Longo, *J. Colloid Interface Sci.*, 2009, **330**, 227–236.
72 V. S. Marques, L. S. Cavalcante, J. C. Sczancoski, A. F. P. Alcântara, M. O. Orlandi, E. Moraes, E. Longo, J. A. Varela, M. Siu Li and M. R. M. C. Santos, *Cryst. Growth Des.*, 2010, **10**, 4752–4768.
73 A. S. Barker Jr., *Phys. Rev.*, 1964, **135**, A742–A747.
74 G. M. Clark and W. P. Doyle, *Spectrochim. Acta*, 1966, **22**, 1441–1447.
75 T. Thongtem, A. Phuruangrat and S. Thongtem, *J. Nanopart. Res.*, 2010, **12**, 2287–2294.
76 L. F. Scatena and G. L. Richmond, *J. Phys. Chem. B*, 2004, **108**, 12518–12528.
77 X. Z. Li, B. Walker and A. Michaelides, *Proc. Natl. Acad. Sci. U. S. A.*, 2011, **108**, 6369–6373.
78 R. Parthasarathi, V. Subramanian and N. Sathyamurthy, *J. Phys. Chem. A*, 2006, **110**, 3349–3351.
79 http://www2.panasonic.com/consumer-electronics/shop/Home-Appliances/.
80 E. L. da Silva, J. A. Varela, D. K. A. Almeida and D. P. Volanti, Microwave aided device for hydrothermal synthesis of nanostructured oxides, particularly obtaining particles of metal oxides, comprises container, in which hydrothermal reaction takes place, and lid for container, Patent Number(s): BR200815393-A2, 07 Dec 2010, p. 19. [Remark 4].
81 G. J. Wilson, A. S. Matijasevich, D. R. G. Mitchell, J. C. Schulz and G. D. Will, *Langmuir*, 2006, **22**, 2016–2027.
82 Q. Yu, H. Lei, G. Yu, X. Feng, Z. Li and Z. Wu, *Chem. Eng. J.*, 2009, **155**, 88–93.
83 M. Godinho, C. Ribeiro, E. Longo and E. R. Leite, *Cryst. Growth Des.*, 2008, **8**, 384–386.
84 A. P. Moura, L. S. Cavalcante, J. C. Sczancoski, D. G. Stroppa, E. C. Paris, A. J. Ramirez, J. A. Varela and E. Longo, *Adv. Powder Technol.*, 2010, **21**, 197–202.
85 S. Liu, S. Tian and R. Xing, *CrystEngComm*, 2011, **13**, 7258–7261.
86 Y. Tian, B. Chen, H. Yu, R. Hu, X. Li, J. Sun, L. Cheng, H. Zhong, J. Zhang, Y. Zheng, T. Yu and L. Huang, *J. Colloid Interface Sci.*, 2011, **360**, 586–592.

87 P. Kubelka and F. Munk-Aussig, *Z. Tech. Phys.*, 1931, **12**, 593–601.
88 A. E. Morales, E. S. Mora and U. Pal, *Rev. Mex. Fis. S*, 2007, **53**, 18–22.
89 R. A. Smith, *Semiconductors*, Cambridge University Press, London, 2nd edn, 1978, p. 434.
90 Y. Zhang, N. A. W. Holzwarth and R. T. Williams, *Phys. Rev. B: Condens. Matter Mater. Phys.*, 1998, **57**, 12738–12750.
91 R. Lacomba-Perales, J. Ruiz-Fuertes, D. Errandonea, D. Martínez-García and A. Segura, *EPL*, 2008, **83**, 37002–37006.
92 L. Chen, H. Hu and Z. Xiong, *Chin. J. Struct. Chem.*, 2013, **1**, 22–26.
93 Z. Xia, J. Zhuang, H. Liu and L. Liao, *J. Phys. D: Appl. Phys.*, 2012, **45**, 015302–015308.
94 M. Nazarov and D. Y. Noh, *J. Rare Earths*, 2010, **28**, 1–11.
95 W. Wang, P. Yang, S. Gai, N. Niu, F. He and J. Lin, *J. Nanopart. Res.*, 2010, **12**, 2295–2305.
96 S. Shi, X. Liu, J. Gao and J. Zhou, *Spectrochim. Acta, Part A*, 2008, **69**, 396–399.
97 Y. Su, L. Li and G. Li, *J. Mater. Chem.*, 2009, **19**, 2316–2322.
98 S. Qi, H. Xie, Y. Huang, S. I. Kim and H. J. Seo, *Opt. Mater. Express*, 2014, **4**, 190.
99 Y. Chen, H. K. Yang, S. W. Park, B. K. Moon, B. C. Choi, J. H. Jeong and K. H. Kim, *J. Alloys Compd.*, 2012, **511**, 123–128.

